Welding in the World
https://doi.org/10.1007/s40194-019-00819-9

RESEARCH PAPER

Thermodynamic simulation of ferritic to ferritic dissimilar metal welds

Fabian Dittrich[1] · P. Mayr[1] · J. A. Siefert[2]

Received: 24 May 2019 / Accepted: 22 October 2019

Abstract
Modern computational calculation power enables scientists to accurately predict the microstructural evolution of complex metallurgical systems and, for example, their phase formation at elevated temperature for an extended amount of time. Valuable information can be derived from those calculations without the necessity of expensive and complicated experiments. Especially the field of power generation, where service parameters strongly influence the applied materials, can benefit from computational simulations. This study will highlight the use of thermodynamic simulations on the behavior of T23 to T91 ferritic dissimilar metal welds (DMWs) at elevated temperatures, similar to creep conditions. The software MatCalc is used to calculate precipitation sequences in the base metals, as well as carbon migration in DMWs from the higher alloyed to the lower alloyed material at elevated temperatures and precipitate distribution across the fusion line of the DMWs. The results of the simulations are verified with creep exposed cross-weld samples (80 MPa, 600 °C, and 625 °C) tested for up to 14,000 h.

Keywords Ferritic steels · Dissimilar materials · Carbon migration · Simulation

1 Introduction

Continuously improving the efficiency of modern fossil-fueled power plants leads to significant progress in the development of creep strength enhanced ferritic (CSEF) steels such as 9 wt% chromium Grade 91 and 2.25 wt% chromium Grade 23. These materials show exceptional creep properties due to a combination of different strengthening mechanisms, such as dispersion hardening, solution hardening, and subgrain boundary hardening. While the bainitic microstructure of the Grade 23 material is strengthened by carbides and carbonitrides formed due to the addition of micro-alloying elements such as vanadium, niobium, carbon, and nitrogen, the strength of the Grade 91 materials lies in its precipitation-strengthened martensitic microstructure [1].

In modern power plants, it is necessary to transition between dissimilar materials over relatively small distances to accommodate different service conditions. Understanding the behavior of dissimilar metal welds (DMW) under creep conditions is a key aspect in supporting best practice fabrication, assessing remaining life and supporting future inspection decisions. Due to the abrupt transition between materials with very different chemical compositions, at elevated service conditions, a phenomenon called uphill-diffusion of carbon from the lower alloyed chromium steel to the one with higher chromium content can be observed [2–5]. This carbon migration is a result of differences in the chemical activity of carbon in the different materials and will lead to permanent changes of the microstructure near the fusion line of both materials used in the DMW. The enrichment of carbon on the higher alloyed side leads to the precipitation of carbides near the fusion line in the carbon enriched zone (CEZ), depleting the surrounding matrix of carbide forming elements such as chromium, altering the properties of this area compared with that of the base metal matrix. However, on the lower alloyed side, the microstructure gets depleted of carbon. A carbon-depleted zone (CDZ) is formed, where all the carbides are dissolved to supply the carbon migration with atoms. Since the carbides in the

F. Dittrich and P. Mayr are formerly affiliated to Chemnitz University of Technology, Chair of Welding Engineering, 09126, Chemnitz, Germany.

✉ Fabian Dittrich
fabian.dittrich@tum.de

[1] Materials Engineering of Additive Manufacturing, Technical University of Munich, 85478 Garching/Munich, Germany

[2] Electric Power Research Institute Inc., 3420 Hillview Avenue, Palo Alto, CA 94303, USA

Published online: 14 November 2019

Table 1 Chemical compositions of the used materials in wt%; Fe balance; n.s. for "not specified"

Material	C	Cr	Mo	V	Mn	Ni	W	Si	N	Nb
Grade 23 dia. 4 mm	0.07	2.33	0.00	0.222	0.61	0.04	1.55	0.24	n.s.	n.s.
Grade 23 dia. 3.2 mm	0.07	2.28	0.01	0.19	0.52	0.08	1.73	0.23	n.s.	n.s.
Grade 23 dia. 2.5 mm	0.07	2.58	0.01	0.207	0.63	0.05	1.6	0.22	n.s.	n.s.
Grade 91 parent	0.11	8.29	0.95	0.2	0.45	0.14	---	0.29	0.0379	0.069
	Al	As	Cu	P	S	Sn	N:Al			
	0.006	0.005	0.16	0.011	0.009	0.01	6:3			

lower alloyed material are a major factor in supporting the martensitic/bainitic microstructure, at elevated temperatures, the microstructure tends to recrystallize to a weaker ferritic crystal structure. These structural changes are observed in a very narrow region of less than 1 mm across the fusion line, resulting in different mechanical properties. This enables intensification of strain localization and increases the susceptibility to damage at service conditions [6, 7].

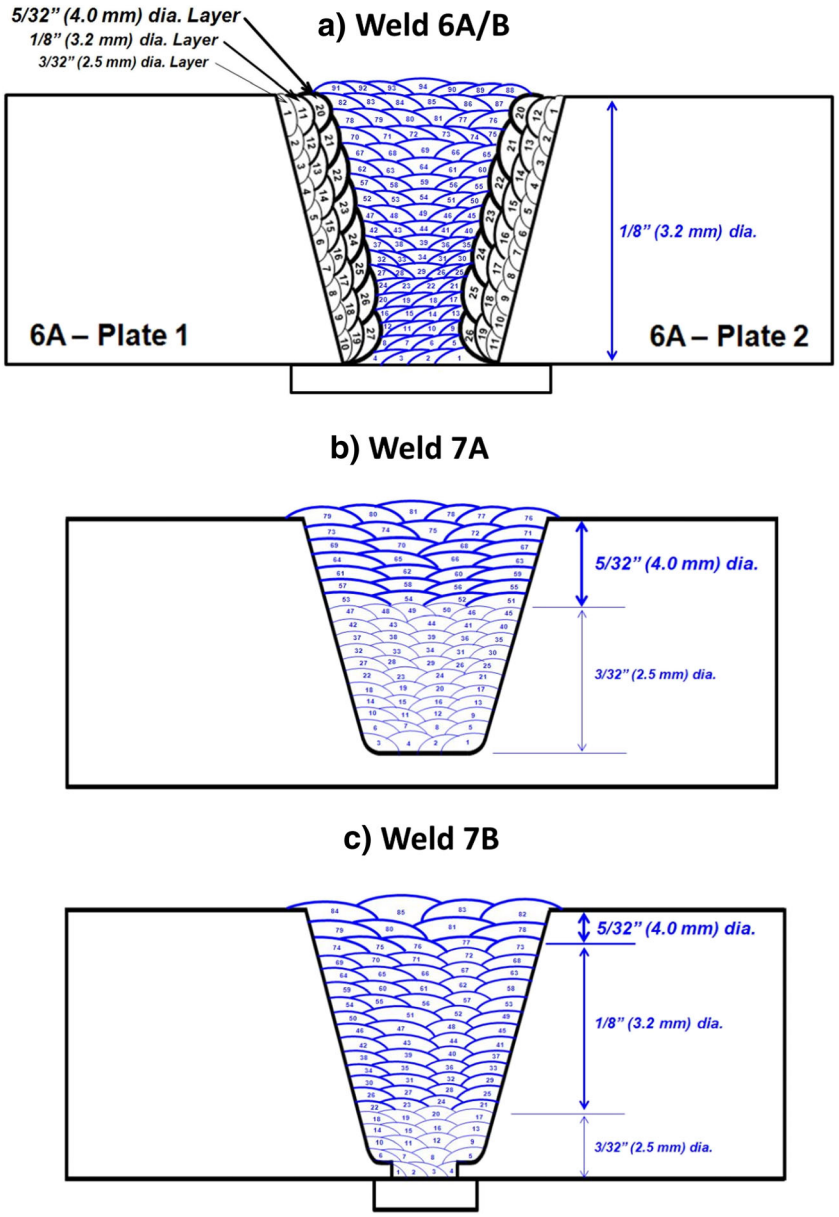

Fig. 1 Schematics of the weld layer sequences for the feature-sized creep samples

Table 2 Recorded weld parameters for the welds 6A/B, 7A, and 7B. The minimum to maximum range values rather than the specific values for amperage, voltage, weld speed, and heat input are given to keep a proper readability of the table

Weld	Dia. (mm)	Pass	Amperage (A)	Voltage (V)	Weld speed (cm/min)	Heat input (kJ/cm)
6A/B flanks	2.5	1&10/1&11	74–78	21–27	17.5–19	5.59–5.98
	3.2	11&19/12&19	111–113	22–24.1	18–19.6	7.52–8.66
	4.0	20&27/20&26	154–157	21–25	17.5–21.3	10.63–12.48
6A/B fill	3.2	1–94	125–126	24–25.2	17.3	10.71
7A fill	2.5	1–20	74–77	21–24	20	5.08
	3.2	21–72	111–113	22.3–25.4	19.6	8.22
	4.0	73–85	125–127	22–24.2	15.2	11.46
7B fill	3.2	1–50	97–98	23.1–24.5	16.3	8.62
	4.0	51–81	125–127	22–24.2	15.2	11.46

2 Experimental procedures

For computational simulations, the software package MatCalc Vers. 5.62 was employed [8]. Equilibrium phase fraction calculations were conducted to get an understanding of the precipitation behavior for the used materials. Since carbon activity differences in the material are responsible for the driving force for carbon migration in DMWs [9], carbon activity calculations were also computed. Furthermore, the diffusion calculations were carried out utilizing a 1-dimensional finite element mesh with 100 elements. It has to be noted that these calculations are purely based on thermodynamic and kinetic information obtained from the applied MatCalc databases (mc_fe_2.058.tdb for thermodynamic equilibrium and mc_fe_2.010.ddb for diffusion calculations), meaning that the calculations were performed without any adjustable parameters. The computations of this paper are based on earlier computations of a different DMW [10].

To verify the accuracy of the calculations, creep-tested cross-weld samples of T91 welded with T23 weld metal were metallographically investigated. The fusion line region between the T23 weld metal and the T91 base material is of particular interest, as this area of material transition is subjected to the most notable microstructure changes during creep exposure. Table 1 summarizes the alloying compositions of the Grade 23 weld metal electrodes that were used, as well as the Grade 91 base material.

The welds were produced via manual shielded metal arc welding (SMAW) using three Grade 23 type weld electrodes ("E9015-G") differing in electrode diameter (2.5 mm, 3.2 mm, 4 mm). Schematics of the weld layer sequences can be seen in Fig. 1. Plate thickness was 48 mm, preheat temperature was set to 150 °C, and the interpass temperature to 315 °C. Table 2 gives an overview over the recorded welding parameters, the numbers in the "Pass"-column corresponds with the numbers of the passes in the layer sequence schematics in Fig. 1. Samples were post weld heat treated (PWHT) at 745 °C for 2 h. Subsequent to welding and PWHT, the samples were machined to enable creep testing. Figure 2 shows the geometry of the feature-sized (macro-) samples for creep testing at 600 °C and 625 °C with an applied stress of 80 MPa.

Following creep exposure, the specimens were cut via EDM. Employing standard metallographic practice, the samples were ground, polished, and etched (Nital, 2%) for optical microscopy and hardness measurements. A Zeiss Axiovert 200 MAT microscope was used for light-optical investigation, and the SEM analysis was conducted on a Zeiss LEO 1400. Hardness according to DIN EN ISO 6507 was measured with a Struers DuraScan 7.

3 Results and discussion

3.1 Computational simulations

With just the chemical composition of the applied material, it is possible to evaluate equilibrium conditions to describe precipitation behavior during cooling of the base metals. MatCalc

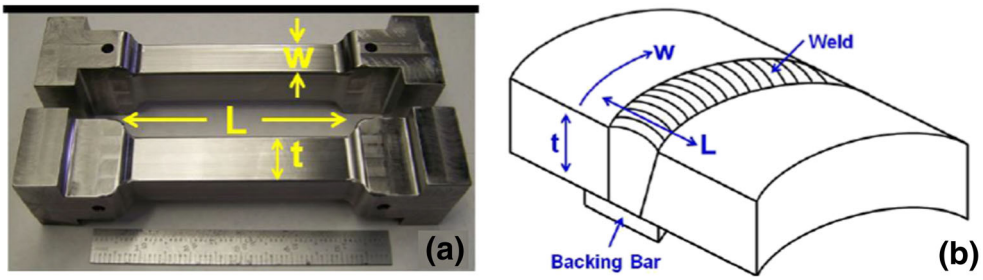

Fig. 2 Machined feature-sized creep specimens (**a**) and relationship of orientation and geometry of the actual weld joint (**b**)

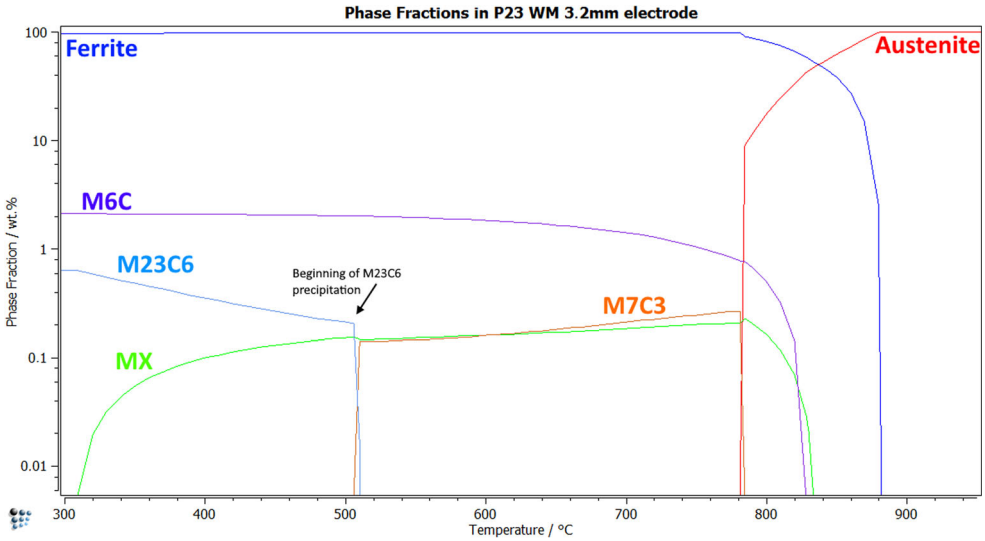

Fig. 3 Equilibrium phase fraction calculation for the Grade 23 weld metal electrode

makes use of the CALPHAD method, enabling the user to incorporate versatile databases for different alloying systems to conduct thermodynamic calculations. This makes it possible to predict material behavior in areas, where no experimental data is available. If the chemical composition of the system is known, a wide variety of different simulations can be computed. To get an idea of the precipitation sequence in the materials, equilibrium phase fractions were simulated. Figure 3 shows the phase fraction diagram for the Grade 23 weld metal.

For the calculations, a wide variety of precipitates was taken into account. Literature review [2, 5, 11–16 reveals that $M_{23}C_6$ carbides and MX carbonitrides are the dominant precipitate species in the investigated materials. However, different investigations also found M_6C as well as M_7C_3 carbides in lower and higher alloyed chromium steels. The correlation between M_7C_3 and $M_{23}C_6$ precipitation is clearly visible in Fig. 3. The simulation suggests that upon cooling, M_7C_3 precipitation sets in when austenite transformed to ferrite. At around 510 °C, the M_7C_3 precipitates are being dissolved in favor of $M_{23}C_6$ carbides. If M_7C_3 carbides are excluded from the calculations, the simulation results show a much earlier onset of $M_{23}C_6$ precipitation at 780 °C (Fig. 4). This example should clarify that the knowledge of precipitates present in the materials is essential for a precise simulation of the material behavior.

The carbon activity calculations in the Grade 91 base metal and the Grade 23 weld metal are the basis of the following carbon migration calculations. Figure 5 shows the results of a carbon activity calculation for the investigated materials. The gap of carbon activity is quite large with over an order of magnitude between the Grade 91 base material and the Grade 23 weld metal electrodes. Interesting to see is that, although the weld metal electrodes have nearly the same

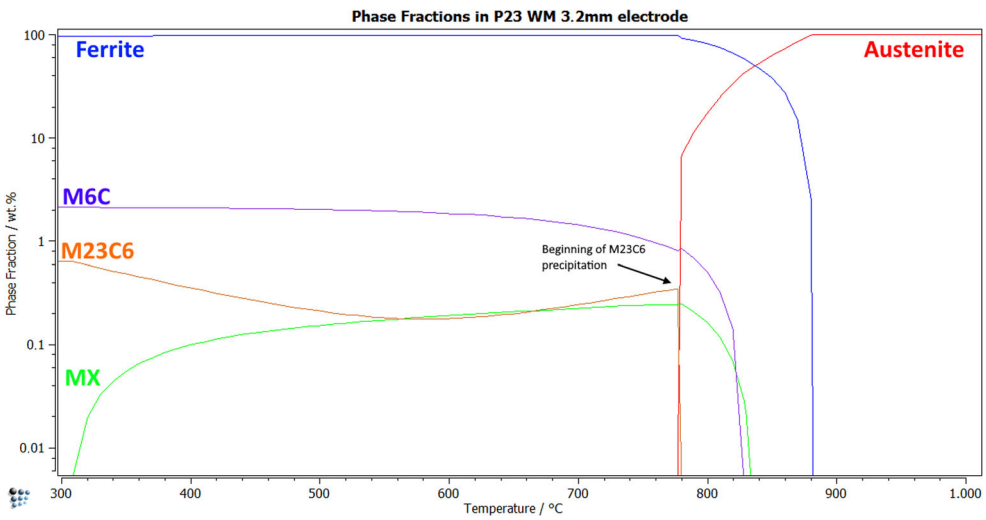

Fig. 4 Equilibrium phase fraction calculation for the Grade 23 weld metal electrode, M_7C_3 carbides excluded

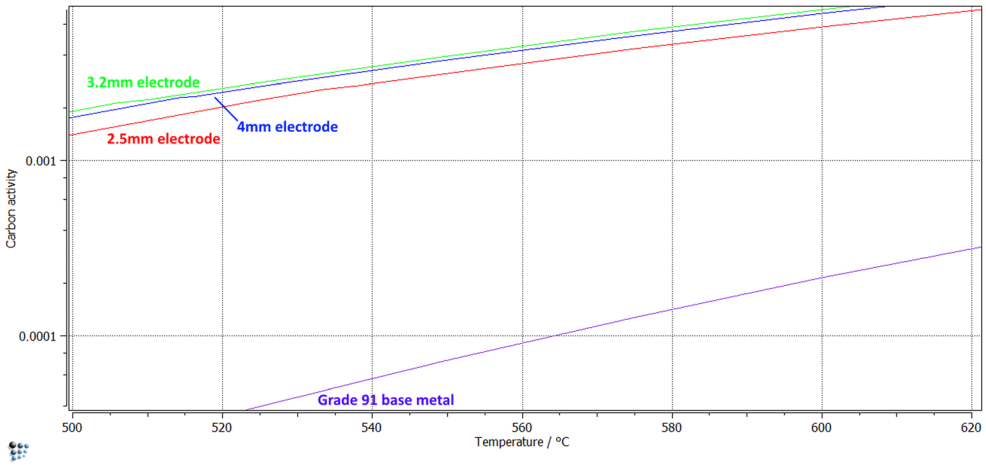

Fig. 5 Calculated carbon activity comparison between the Grade 91 base material and the different Grade 23 weld metal electrodes

chemical composition, there are distinguishable differences in their carbon activities.

Taking the chemical composition differences of the weld metal electrodes into account, it is interesting to explore the possibility of closing the carbon activity gap by varying the chemical compositions in such a way that the defined elemental boundaries (see Table 3) are still met for the materials [17, 18]. If it is possible to close, or at least considerably narrow the gap in carbon activity by adjusting the content of the alloying elements, then the driving force for carbon migration will also decrease.

At first, the influence of the specific elements on carbon activity needs to be evaluated. This can be done by varying the element content of a single element in its given boundaries, while keeping the other elements set in their content. Plotting the carbon activity over the element content gives information on the influence of each element on carbon activity in the material (compare Fig. 6).

From the calculations, it can be derived that in order to decrease the carbon activity of Grade 23 material, element contents of Cr, W, V, Mo, and Nb have to be increased while the element contents of C, N, and B need to decrease. The same can be done for Grade 91 material in order to raise the carbon activity. The result of the procedure is shown in Fig. 7. It is not quite possible to close the carbon activity gap between Grade 91 and Grade 23 material completely. But if the ratio of carbon activity for example at 550 °C is compared—T23/T91 has a ratio of 51.25 (big gap) and T23v/T91v (materials with a tailored composition that is aimed to reduce the carbon activity difference) has a ratio of 3.33 (small gap)—it is possible to reduce the carbon activity ratio by a factor of 15, which should lead to significantly reduced driving force for the carbon migration.

Diffusion calculation enables the prediction of the carbon migration across the weld for a given time at elevated service conditions, possibly making such calculations a valuable tool for remaining life assessments in the power generation industry. Figure 8 shows an example of plotting the carbon content over the specimen length (upper plot). This is the predicted carbon content after 2320 h at 625 °C in the simulated weld metal produced using a 3.2-mm diameter Grade 23 electrode. Carbon content peaks on the higher alloyed side of the DMW at around 0.3 wt%, while a carbon depletion on the Grade 23 weld metal side is clearly visible. The diagram at the bottom of the picture depicts the corresponding phase fraction evolution of the precipitates. The increase in carbon content directly correlates with the precipitation of $M_{23}C_6$ carbides according to the simulations. The carbon depletion on the weld metal side leads to a breakdown of M_7C_3 and MX particles. This is also the location where the martensitic/bainitic microstructure will most likely transform into ferrite crystals, since supporting particles are not present anymore. The findings of the simulation are

Table 3 Chemical composition boundaries (minimum and maximum allowable content) for Grade 23 and Grade 91 material in wt% according to [17, 18]

	C	Mn	Cr	Mo	Si	Ni	V	N	Nb/Ti
Grade 91	0.08–0.12	0.3–0.6	8.0–9.5	0.85–1.05	0.2–0.5	< 0.4	0.18–0.25	0.03–0.07	0.06–0.1
	C	Mn	Cr	Mo	Si	Nb	V	N	W
Grade 23	0.04–0.1	0.1–0.6	1.9–2.6	0.05–0.3	< 0.5	0.02–0.08	0.2–0.3	< 0.03	1.45–1.75

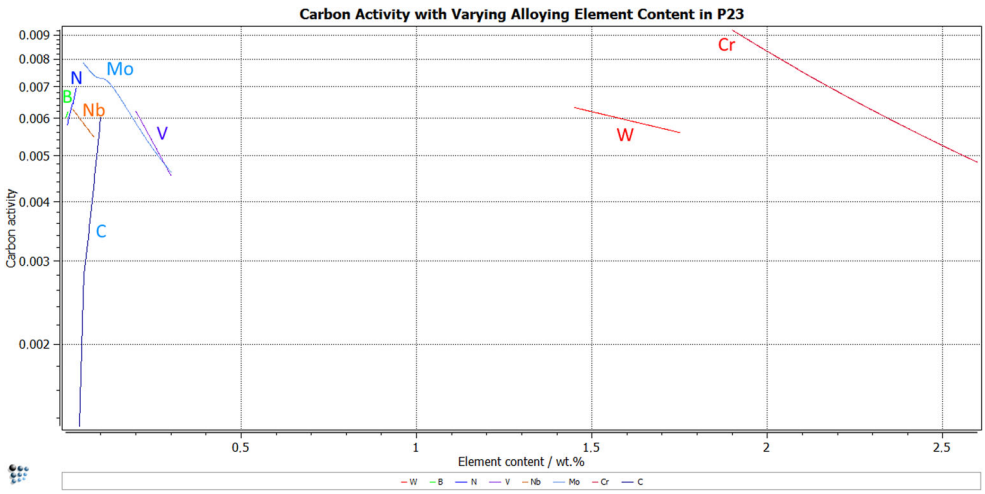

Fig. 6 Influence of varying element content on the carbon activity of Grade 23 material

in good agreement with the microstructural analysis (compared with Section 3.2).

3.2 Metallographic investigation

To verify the results acquired via simulations, microstructural investigations in the vicinity of the fusion line with a light-optical microscope and SEM analysis were carried out. The applied stress and the elevated temperature resulted in unfavorable microstructural changes due to a directed carbon migration from the lower alloyed weld metal to the higher alloyed base material. As previously stated, the carbon depletion leads to the dissolution of microstructure-stabilizing carbides in the Grade 23 weld metal which results in unwanted recrystallized ferrite in the carbon-depleted zone (CDZ). This can be observed in creep exposed samples as seen in Fig. 9.

SEM images further reinforce these findings (compare Fig. 10). The image was taken with the secondary electron (SE) detector of the SEM. On the T91 side, small finely distributed carbides can be observed, while on the T23 side, rather coarse structures are visible. The formation of fine particles in the Grade 91 material leads to a local increase in the hardness adjacent to the fusion line, where on the contrary in the lower alloyed weld metal, the carbon depletion weakens the microstructure and makes it softer. The coarse white particles on the Grade 23 weld metal side were analyzed using EDS analysis and identified to be tungsten-rich Laves phase.

Microstructural analysis showed that the recrystallization in the weld metal microstructure is only partial, meaning only isolated ferrite islands can be observed at the fusion line. This is attributed to the strengthening micro-alloying additions as well as the relatively short testing times (1000 to 10,000 h). The data acquired with regard to the ferritic recrystallization is summarized in Table 4. It is notable that the condition of the Grade 91 base material seems to affect the diffusion and ultimately the recrystallization behavior of the weld metal as well. The "A"-samples were manufactured using untreated ex-service material, while for the "B"-samples, the Grade 91 material was renormalized and tempered prior to welding.

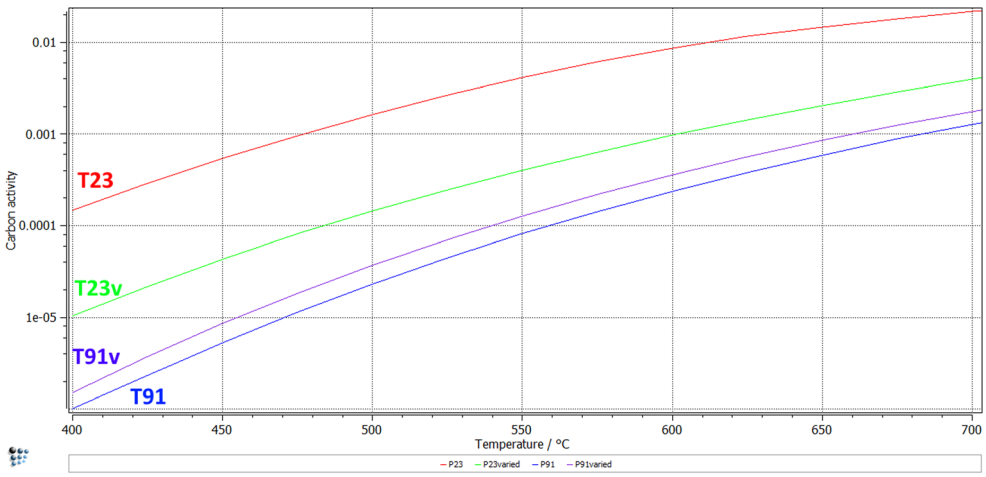

Fig. 7 Carbon activity comparison for the investigated materials (T23 and T91) and materials with a tailored chemical composition that is aimed to reduce the carbon activity difference (T23v and T91v)

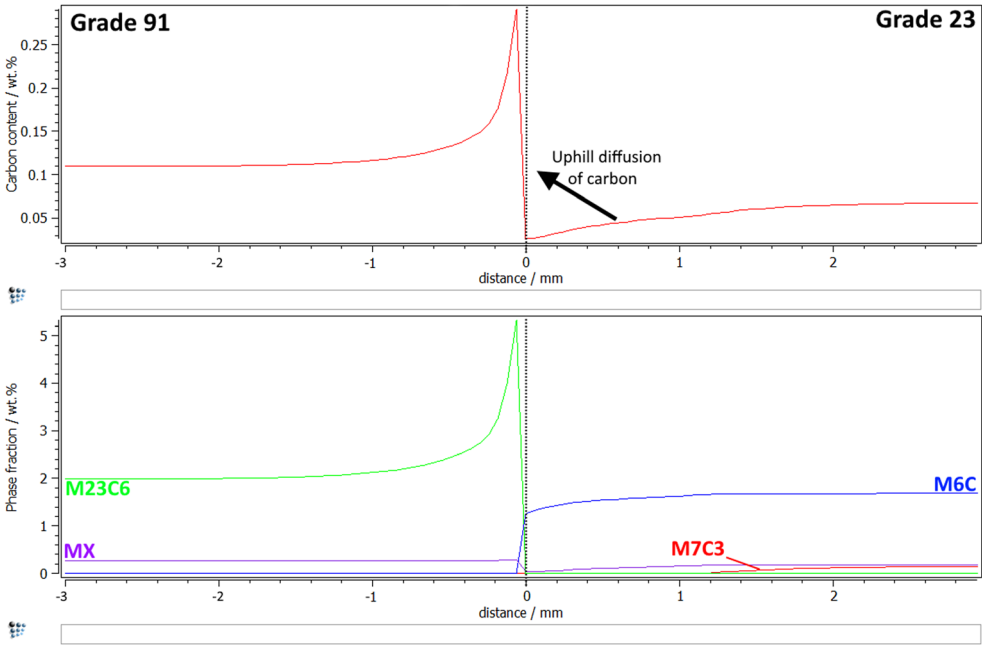

Fig. 8 Diffusion calculation over the fusion line of a Grade 91 to Grade 23 DMW. Upper plot shows the carbon content after a simulated exposure of 2350 h at 625 °C. Bottom diagram shows the corresponding response of phase fraction evolution of the different precipitates. The dotted line at 0 mm indicates the fusion line

The renormalized and tempered samples show distinctively more recrystallization after creep exposure, although the testing time was shorter in both cases. This can be attributed to the fact that the normalization treatment reduces the amount of dislocations in the microstructure. By exposing the sample to elevated temperatures during creep exposure, more dislocations can be generated and pile up, which leads to faster recrystallization.

3.3 Hardness measurements

Hardness was measured to investigate the effect of PWHT as well as the creep exposure on the welded joints. Table 5 summarizes all accumulated data. In the as-welded condition, the base metal hardness correlates to its starting condition—renormalized and tempered Grade 91 base material appears to be slightly harder than the ex-service ("A") sample. The weld metal does not show a significant difference. After PWHT, the weld metal hardness drops 113 HV10 and 128 HV10 for the "A"- and "B"- samples, respectively. The renormalized and tempered base metal specimen showed a stronger reaction to PWHT with a drop of 38 HV10, while the "A"- sample only slightly decreased its hardness by 22 HV10. The diagram in Fig. 11 was generated by conducting a microhardness line scan (HV0.05) across the fusion line of the sample 7A-2. On the weld metal side, a very distinct hardness drop with a width of around 100 µm is visible

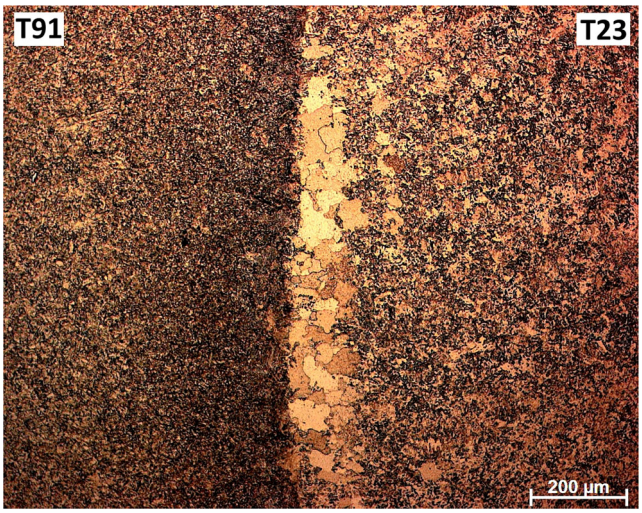

Fig. 9 Partially recrystallized microstructure along the fusion line in the Grade 23 weld metal creep exposed for 2314 h at 625 °C

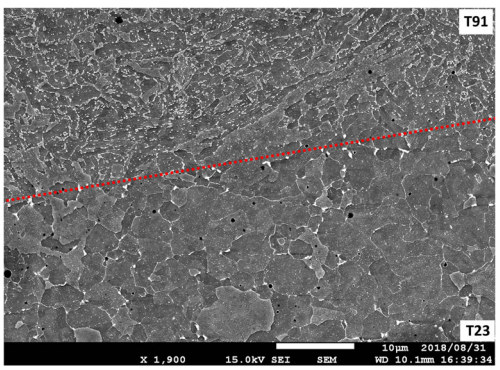

Fig. 10 SEM picture of a creep exposed (600 °C for 7347 h) Grade 91 (T91) to Grade 23 (T23) DMW. SE image, red dotted line indicates the fusion line

Table 4 Measured average width and the standard deviation of recrystallized material, as well as the percentage of recrystallization in relation to the weld line length. RFZ stands for recrystallized ferrite zone

Sample ID	Temperature / °C	Time to rupture / h	Average width of the RFZ / μm	Standard deviation	Percentage of recrystallized microstructure / %
7A-1	625	2314	127	23	10.5
7B-1		1326	109	10	29.6
7A-2	600	9442	138	38	2.1
7B-2		7347	131	16	13.3

that correlates well with the width of the recrystallized microstructure. Crossing the fusion line, a very sharp increase of the hardness is observed that is attributed to the finely distributed carbides that precipitated there due to the migration of carbon (carbon enriched zone (CEZ)). This line scan further reinforces the observations of the microstructural analysis as well as the results of the computational simulations.

4 Conclusions

The present study aimed to portray the possibilities which thermodynamic simulation software provides with regard to predicting the behavior of creep exposed dissimilar metal welds. Basing the thermodynamic calculations on the chemical composition makes it possible to predict precipitation sequences during the cooling of the material under equilibrium conditions. These results are valuable assets for more complicated calculations, such as 1-dimensional diffusion simulations with simulation parameters matching creep experiments or service conditions. Carbon migration calculations showed the extent of carbon depletion in the lower alloyed material and carbon enrichment in the higher alloyed material under conditions similar to actual creep exposure tests. Carbon activity calculations were conducted that showed the extent of the difference between high chromium and lower chromium steels. Furthermore, a practical example was given on how such element activity calculations can be applied for alloying optimization.

Microstructural investigations of creep exposed T91 to T23 DMWs were able to show the undesired microstructural changes that such welded joints undergo under service conditions. Partial recrystallization of the weld metal microstructure due to the dissolution of carbides in the carbon-depleted zone was observed. Furthermore, on the higher alloyed Grade 91 base metal side, finely distributed carbides were found that correlate to a dramatic increase in hardness right next to the fusion line of the weld. The analysis of the results and the comparison with the data accumulated with 1-dimensional diffusion simulations showed reasonable agreement between the computational simulations and the creep experiments. It was also shown that in order to achieve improved results from the computational simulations, it is necessary to know the materials involved and their exact microstructural features—namely their inherent precipitate phases.

Table 5 Summary of collected hardness measurement data. WM Grade 23 weld metal, BM Grade 91 base metal

Sample	As welded			
	7A BM	7A WM	7B BM	7B WM
Hardness / HV 10	206	323	260	352
Sample	After PWHT			
	7A BM	7A WM	7B BM	7B WM
Hardness / HV 10	184	210	222	224
Sample ID	After creep exposure			
	7A-1 BM	7A-1 WM	7B-1 BM	7B-1 WM
Hardness / HV 10	184	190	215	216
Sample ID	7A-2 BM	7A-2 WM	7B-2 BM	7B-2 WM
Hardness / HV 10	182	192	207	195

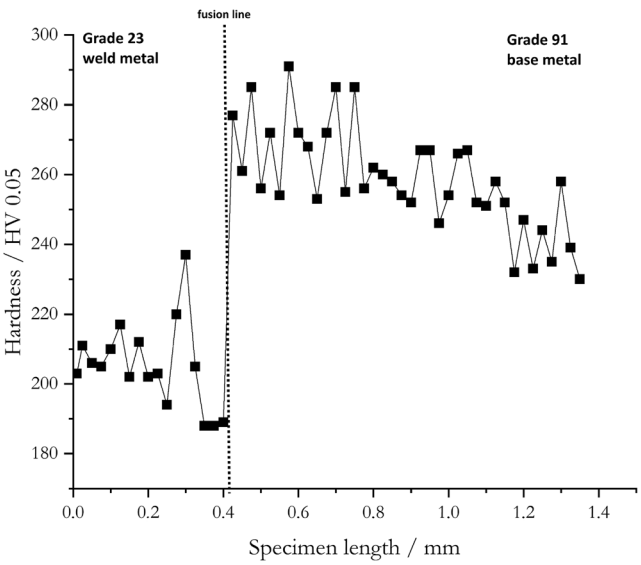

Fig. 11 Microhardness line scan across the fusion line of the sample 7A-2, through an area of recrystallized material

The computational simulations employed in this study proved to be a valuable tool in predicting the behavior of ferritic to ferritic dissimilar metal welds.

References

1. Vaillant JC, Vandenberghe B, Hahn B, Heuser H, Jochum C (2008) T/P23, 24, 911 and 92: new grades for advanced coal-fired power plants – properties and experience. Int J Press Vessel Pip 85:38–46. https://doi.org/10.1016/j.ijpvp.2007.06.011
2. Anand R, Sudha C, Saroja S, Vijayalakshmi M (2013) Experimental and thermokinetic simulation studies on the formation of deleterious zones in dissimilar ferritic steel weldments. Metall Mater Trans A 44A:2156–2170. https://doi.org/10.1007/s11661-012-1591-9
3. Dawson KE (2012) Dissimilar metal welds. Dissertation, University of Liverpool
4. Sudha C, Terrance ALE, Albert SK, Vijayalakshmi M (2002) Systematic study of formation of soft and hard zones in the dissimilar weldments of CrMo steels. J Nucl Mater 302:193–205. https://doi.org/10.1016/S0022-3115(02)00777-8
5. Sudha C, Thomas Paul V, Terrance ALE, Saroja S, Vijayalakshmi M (2006) Microstructure and microchemistry of hard zone in dissimilar weldments of Cr-Mo steels. Weld J:71–80
6. Thomas A, Pathiraj B, Veron P (2007) Feature tests on welded components at higher temperatures – material performance and residual stress evaluation. Eng Fract Mech 74:969–979. https://doi.org/10.1016/j.engfracmech.2006.08.017
7. Wang Y, Li L (2016) Microstructure evolution of fine-grained heat affected zone in type IV failure of P91 welds. Weld J 95:27–36
8. E. Kozeschnik: MatCalc (Materials Calculator); software available at https://www.matcalc-engineering.com/index.php. Accessed 20 Oct 2019
9. Darken LS (1949) Diffusion of carbon in austenite with a discontinuity in composition. Trans AIME 180:430–438
10. Dittrich F, Mayr P, Martin D, Siefert JA (2018) Characterization of an ex-service P22 to F91 ferritic dissimilar metal weld. Weld World 62:793–800. https://doi.org/10.1007/s40194-018-0569-7
11. Strilkova L, Kubon Z, Vodarek V (2010) Creep failure characteristics in P23/P91 dissimilar welds. Conference Paper - METAL 2010
12. Amsupan S, Consonni M, Poopat B, Sirivedin K (2015) Influence of the welding heat cycle on the HAZ properties of T23 joints. Int J Inst Mater Malays 2-1:233–249
13. Dawson K, Tatlock G (2011) The stability of fine, sub-grain microstructures within carbon depleted regions of dissimilar metal, ferritic, creep resistant welds. ASME 2011 pressure vessels and piping conference. https://doi.org/10.1115/PVP2011-57868
14. Laha K (2014) Integrity assessment of similar and dissimilar fusion welded joints of Cr-Mo-W ferritic steels under creep condition. Proc Eng 86:195–202. https://doi.org/10.1016/j.proeng.2014.11.028
15. Foret R, Zlamal B, Sopousek J (2006) Structural stability of dissimilar weld between two CrMoV steels. Weld J:211–217
16. Vodarek V, Kubon Z, Foret R, Hainsworth SV (2008) Microstructural evolution in P23/P91 heterogeneous welds during creep at 500-600°C. Safety and reliability of welded components in energy and processing industry proceedings of the IIW international conference, pp 233–238
17. Case 2199: 9Cr-1Mo-1W-Cb Material, Cases of American Society of Mechanical Engineers Pressure Vessel, Code Case 2199–6, 2011
18. DIN EN 10302:2008–06 – Creep resisting steels, nickel and cobalt alloys